

Statistical characterization of high-to-medium frequency mesoscale gravity waves by lidar-measured vertical winds and temperatures in the MLT



Xian Lu^{a,d,*}, Xinzhao Chu^{a,b,*}, Haoyu Li^{a,b}, Cao Chen^{a,b}, John A. Smith^a, Sharon L. Vadas^c

^a Cooperative Institute for Research in Environmental Sciences, University of Colorado at Boulder, USA

^b Department of Aerospace Engineering Sciences, University of Colorado at Boulder, USA

^c NWRRA, Boulder, CO, USA

^d Department of Physics and Astronomy, Clemson University, Clemson, SC, USA

A B S T R A C T

We present the first statistical study of gravity waves with periods of 0.3–2.5 h that are persistent and dominant in the vertical winds measured with the University of Colorado STAR Na Doppler lidar in Boulder, CO (40.1°N, 105.2°W). The probability density functions of the wave amplitudes in temperature and vertical wind, ratios of these two amplitudes, phase differences between them, and vertical wavelengths are derived directly from the observations. The intrinsic period and horizontal wavelength of each wave are inferred from its vertical wavelength, amplitude ratio, and a designated eddy viscosity by applying the gravity wave polarization and dispersion relations. The amplitude ratios are positively correlated with the ground-based periods with a coefficient of ~ 0.76 . The phase differences between the vertical winds and temperatures ($\varphi_w - \varphi_T$) follow a Gaussian distribution with $84.2 \pm 26.7^\circ$, which has a much larger standard deviation than that predicted for non-dissipative waves ($\sim 3.3^\circ$). The deviations of the observed phase differences from their predicted values for non-dissipative waves may indicate wave dissipation. The shorter-vertical-wavelength waves tend to have larger phase difference deviations, implying that the dissipative effects are more significant for shorter waves. The majority of these waves have the vertical wavelengths ranging from 5 to 40 km with a mean and standard deviation of ~ 18.6 and 7.2 km, respectively. For waves with similar periods, multiple peaks in the vertical wavelengths are identified frequently and the ones peaking in the vertical wind are statistically longer than those peaking in the temperature. The horizontal wavelengths range mostly from 50 to 500 km with a mean and median of ~ 180 and 125 km, respectively. Therefore, these waves are mesoscale waves with high-to-medium frequencies. Since they have recently become resolvable in high-resolution general circulation models (GCMs), this statistical study provides an important and timely reference for them.

1. Introduction

Due to significantly improved optical efficiency (Smith and Chu, 2015), the University of Colorado Student Training and Atmosphere Research (STAR) Na Doppler lidar can now measure vertical winds in the mesosphere and lower thermosphere (MLT) with high precision and resolution (Smith and Chu, 2015; Lu et al., 2015a). At the Table Mountain Lidar Observatory (40.1°N, 105.2°W) north of Boulder, Colorado, the most salient and persistent features in the vertical wind field, measured with this STAR lidar, are gravity waves with periods of 0.3–2.5 h. Such high-to-medium frequency waves are also discernable in the temperature field, and contribute significantly to its short-term variability. The simultaneous observations of monochromatic, 0.3–2.5 h MLT gravity waves in both the vertical wind and temperature

were rare in previous studies (e.g., Collins et al., 1994; Hu et al., 2002; Gavrilo et al., 1996; Riggini et al., 1997; Taylor et al., 1997; Walterscheid et al., 1999; Suzuki et al., 2004; Li et al., 2011; Chen et al., 2016). In addition, we employ the amplitude ratios of the relative temperature to vertical wind in order to infer the intrinsic period and horizontal wavelength from the measured vertical wavelength using the wave polarization relation with and without dissipation. The current study not only demonstrates the utility of simultaneous vertical wind and temperature measurements in the MLT region, but also provides a method by which to infer these two important wave parameters, i.e., the intrinsic period and horizontal wavelength, without knowledge of the background wind field.

The other science merit of this work stems from the fact that the 0.3–2.5 h waves fall into the mesoscale range horizontally, and have

* Corresponding authors at: Cooperative Institute for Research in Environmental Sciences, University of Colorado at Boulder, USA
E-mail addresses: xian@clemson.edu (X. Lu), xinzhao.chu@colorado.edu (X. Chu).

<http://dx.doi.org/10.1016/j.jastp.2016.10.009>

Received 22 July 2016; Received in revised form 11 October 2016; Accepted 14 October 2016

Available online 18 October 2016

1364-6826/ © 2016 Elsevier Ltd. All rights reserved.

Table 1
Statistics of the Lidar data from April 2013 to January 2014 used for this study.

	April	May	June	July	August	September	October	November	December	January	Total
Night	2	3	3	1	7	3	8	8	7	14	56
Hour (h)	15.9	18.5	12.9	6.9	42.2	23.0	73.1	73.6	69.2	125.5	460.8

vertical wavelengths of mainly ~ 10 – 30 km. Such a wave spectrum is different from, and only partially overlaps with, the short-period and small-scale waves (usually < 100 km in horizontal wavelength) preferentially observed by airglow imagers and the long-period and large-scale waves readily detected by less sensitive lidars and radars. The significance of such high-to-medium frequency mesoscale gravity waves on precipitation patterns, weather systems, and the transport of momentum to the MLT region has been widely appreciated (e.g., Koch and O’Handly, 1997; Zhang, 2004; Fritts and Nastrom, 1992), although the direct observations of them were sparse. Therefore, an observational and statistical characterization of the gravity waves with these scales is required. Additionally, recent gravity-wave-resolving, high-resolution GCMs (e.g., Watanabe and Miyahara, 2009; Becker, 2009; Sato et al., 2012; Liu et al., 2014) can resolve mesoscale gravity waves with periods of 0.3–2.5 h directly from the physical processes simulated in the models. Therefore, obtaining information about the characteristics of these waves from an observational standpoint, as done in this study, is important and timely.

In a case study by Lu et al. (2015a), we developed a systematic method to study the characteristics of a quasi-1-h wave using the STAR lidar in Boulder, CO and a Na Doppler lidar and Advanced Mesospheric Temperature Mapper (AMTM) in Logan, UT. The horizontal and vertical wavelengths of this wave were determined to be $\sim 219 \pm 4$ and 16.0 ± 0.3 km, respectively. Because the Utah State University (USU) lidar does not have vertical wind measurements currently, we utilize the STAR lidar observations only for the current statistical study, and analyze the period from April 2013 through January 2014. During this period, there were 56 nights of observations totaling ~ 461 h of high-quality vertical wind measurements (Table 1). The 0.3–2.5 h waves occur and dominate in almost every night of the observations. This dataset therefore provides a compelling opportunity for a statistical study of high-to-medium frequency mesoscale gravity waves.

2. Observations and methodology

2.1. Vertical wind measurements showing prominent 0.3–2.5 h waves

The University of Colorado STAR Na Doppler lidar saves raw photon count profiles with a resolution of 3 s temporally and 24 m vertically. In order to increase the signal-to-noise ratio, the raw photon counts are smoothed with a 15 min (full width) Hamming window to derive temperatures and vertical winds, and the window is shifted at a step of ~ 5 min. Vertically, the photons counts are binned to 0.96 km to further increase the precision. Therefore, the effective temporal and vertical resolutions are 7.5 min and 0.96 km, respectively. With this resolution, the measurement uncertainties in the STAR temperatures and vertical winds are ~ 0.3 – 1 K and ~ 0.2 – 1 m/s near the Na layer peak and the uncertainties in the winter months are usually smaller than those in the summer months due to the higher winter Na abundance. Taking the 27 November 2013 case as an example, the STAR lidar obtained 1000 counts per laser shot from the Na layer with an average laser power of ~ 500 mW at a 30 Hz repetition rate and with a telescope primary mirror of ~ 80 cm in diameter (Lu et al., 2015a).

Fig. 1 illustrates examples of the raw vertical wind measurements at resolutions of 7.5 min and 0.96 km. The most prominent waves are those with high to medium frequencies. The downward progression of their phases indicates that these signatures are real and are created by

upward-propagating gravity waves with upward energy propagation. To obtain the gravity wave perturbations, we first subtract the nightly mean temperatures and vertical winds. Then, to effectively remove the anomalous vertical stripes found in some of our raw vertical winds and the wave spectra with unwanted long periods, we apply the two-dimensional (2D) Fast Fourier Transform (FFT) filtering with zero-padding to remove the vertical wavenumbers close to zero and the periods longer than 3 h. This 2DFFT filtering is fulfilled via the following two steps. First, we derive the 2DFFT spectra that only keep the powers contributed by waves with upward energy propagation, vertical wavenumbers ranging from 0.0081 to 0.5 km^{-1} and frequencies from $1/0.25$ to $1/3 \text{ h}^{-1}$. The lowest wavenumber at 0.0081 km^{-1} is determined by the vertical window width after zero padding (~ 123 km). Second, an inverse 2DFFT is then applied to recover the filtered wave perturbations that are used later to discern the dominant waves and their durations via wavelets. This filtering process selects the waves with periods of 0.25–3 h and vertical wavelengths of 2–123 km. Fig. 2b shows an example of the vertical wind field after this 2DFFT filtering on 10 August 2013. A superposition of multiple upward propagating waves with periods of 0.3–2.5 h is clearly seen.

2.2. Identifying wave cases using wavelet spectra

According to the Boussinesq, non-dissipative gravity wave polarization relation between the vertical wind and temperature perturbations, their amplitude ratio is approximately proportional to wave’s intrinsic frequency (e.g., Eq. (2) in Lu et al., 2015a),

$$\tilde{T} \approx -\frac{iN^2}{g\hat{\omega}} \tilde{w} \quad (1)$$

where \tilde{T} and \tilde{w} are the complex amplitudes of relative temperature and vertical wind, respectively, $\hat{\omega}$ is the intrinsic frequency and N is the Brunt–Väisälä frequency. The Boussinesq approximation holds for $\lambda_z < 4\pi H$, where H is the density scale height (see Eq. (B18) of Vadas (2013) with the substitution i for $-i$ because of the different phase definition). We first calculate the Morlet wavelet spectra of \tilde{T} and \tilde{w} using the method in Chen et al. (2016) and Chen and Chu (2016), where the bias (found in favor of the low-frequency waves) in the 1-D Morlet wavelet power spectrum code by Torrence and Compo (1998) is corrected. Then following the case study by Lu et al. (2015a), the amplitudes of the temperature wavelet spectra are weighted by their observed frequencies (i.e., multiplied by the frequencies) in order to be comparable with the amplitude spectra for the vertical wind and highlight the high-frequency waves, which are the focus of this study. Fig. 2c, d show how we identify the dominant waves and their durations using the vertically averaged wavelet spectra. The local peaks are first identified from these averaged spectra. If two adjacent peaks are within 3 wave cycles, they are treated as the same wave. For example, on the night of 10 August 2013 (Fig. 2d), two local peaks at 8.99 and 9.07 UT with a period of ~ 0.37 h are so close to each other that they are considered as the same peak/wave in our analysis.

To establish a wave case, the same wave peaks must be identified simultaneously in both the temperature and vertical wind perturbations. We allow the periods of these peaks for these two components to differ by no more than 20% of their mean; this mean is then used as the period determined from the wavelet. If the wave’s amplitude distribution along the wavelet time axis is central symmetric, we expand the time window from this peak to both the left and the right sides for

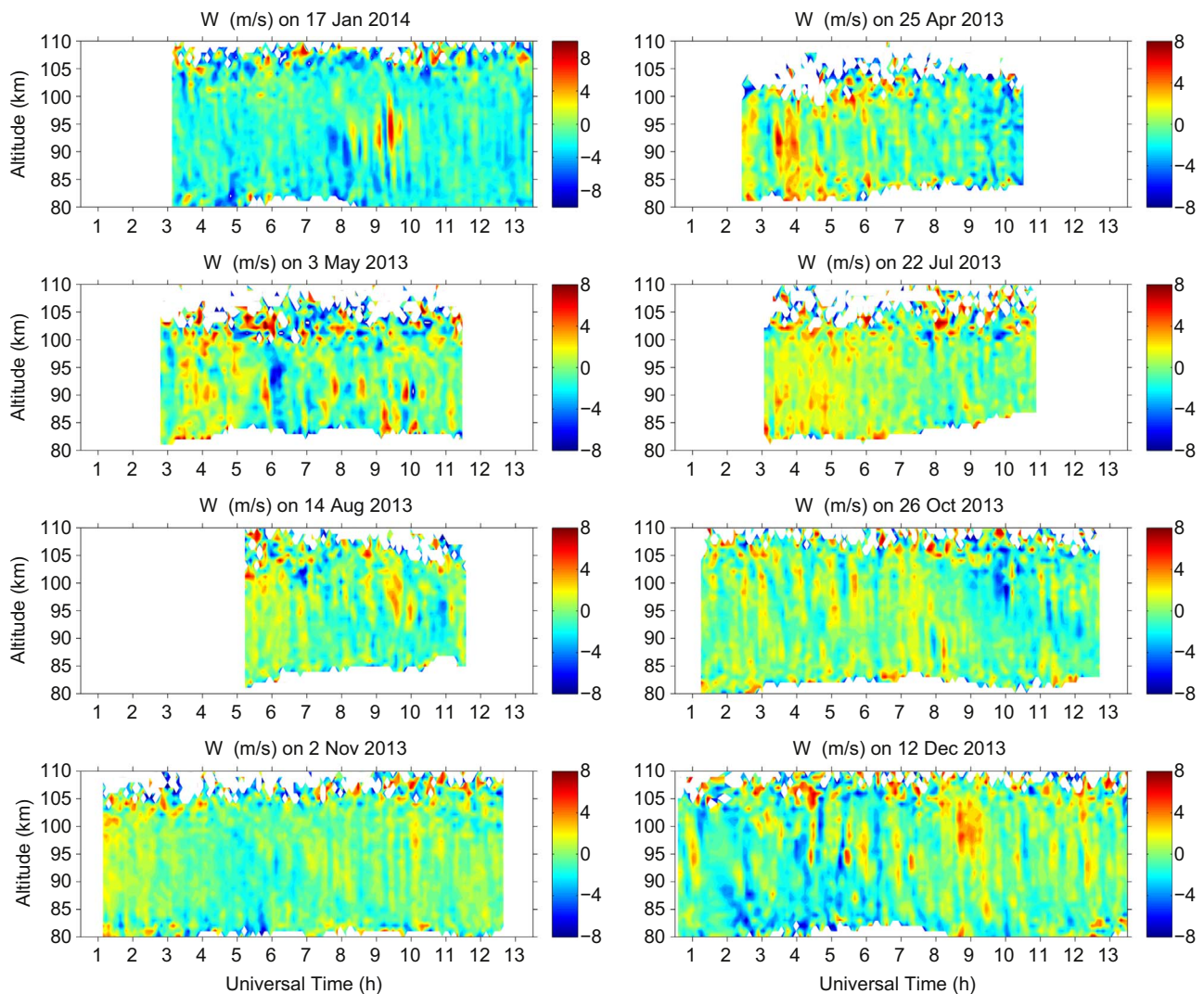


Fig. 1. Examples of raw vertical wind measurements with resolutions of 7.5 min and 0.96 km that show prominent high-to-medium frequency gravity waves.

~1.5–2 wave cycles and regard this window as the duration of the wave, which therefore lasts about 3–4 wave cycles. Using a uniform window width of ~3–4 wave cycles for every wave avoids a bias in the estimation of the wave amplitude which usually relies on a sinusoidal fitting that employs a constant wave frequency. As the wave amplitude, phase, or period changes with time, the fitted amplitude is always larger with a shorter fitting window, and vice versa. In addition, approximately 3–4 wave cycles are long enough to derive the phase accurately. If the wave amplitude distribution is asymmetric, we use the wavelet amplitude to determine the wave duration using the principle that the wave amplitudes should be larger within the window than outside. We also require that the wave peaks exist for at least 2/3 of the available altitude range. We divide the altitude ranges into three regions (i.e., 84.5–89.5, 89.5–94.5, 94.5–99.5 km) and calculate the averaged amplitude spectra individually. Wave peaks that occur in only one of these regions are not taken into account, following the practice in Chen et al. (2016). For example, on the night of 10 August 2013, this last criterion discards the peak at ~0.5 h occurring from ~6 to 8 UT in the mean spectra (Fig. 2c and d).

Using the above procedures, 6 wave cases are identified in the 10 August 2013 data (Table 2) and, in most nights, 3–7 wave cases are identified. A total number of 257 cases are identified from 56 nights of lidar observations during the 10-month period. We note that, using the night of 10 August 2013 as an example, we cannot exclude the possibility that the 0.37-h (occurring at ~9 UT) and 0.38-h (occurring

at ~11 UT) waves might have originated from the same wave packet since their periods are so similar, and therefore were likely excited by the same source. However, we count them as two separate waves here because their magnitudes weakened considerably for a couple of hours between their occurrences. There are several possible explanations for the temporal variation of the wave magnitudes, such as interactions with other waves, modulations by background wind, and/or changes in source strengths. Instead of studying the physical nature and source of each wave, the focus of our study is to identify waves when they are strong locally and study their statistical properties.

2.3. Determining wave amplitude ratios, phase differences, and vertical wavelengths

To determine the wave amplitude and phase, researchers typically apply a 1-D sinusoidal fitting with a known wave frequency at each altitude, then derive the vertical wavelength from the vertical variation of the wave phase (e.g., Lu et al., 2009; Chen et al., 2013). This 1-D fitting method fails to employ any a priori constraint on the vertical wavelength and is not optimal for the current study since the dominant vertical wavelengths in the temperature and vertical wind fields are not always identical. In this case, the amplitude ratios and phase differences of temperature and vertical wind cannot be used in conjunction with the gravity wave polarization relation because this relation can only be applied to the parameters for a single wave, which must have

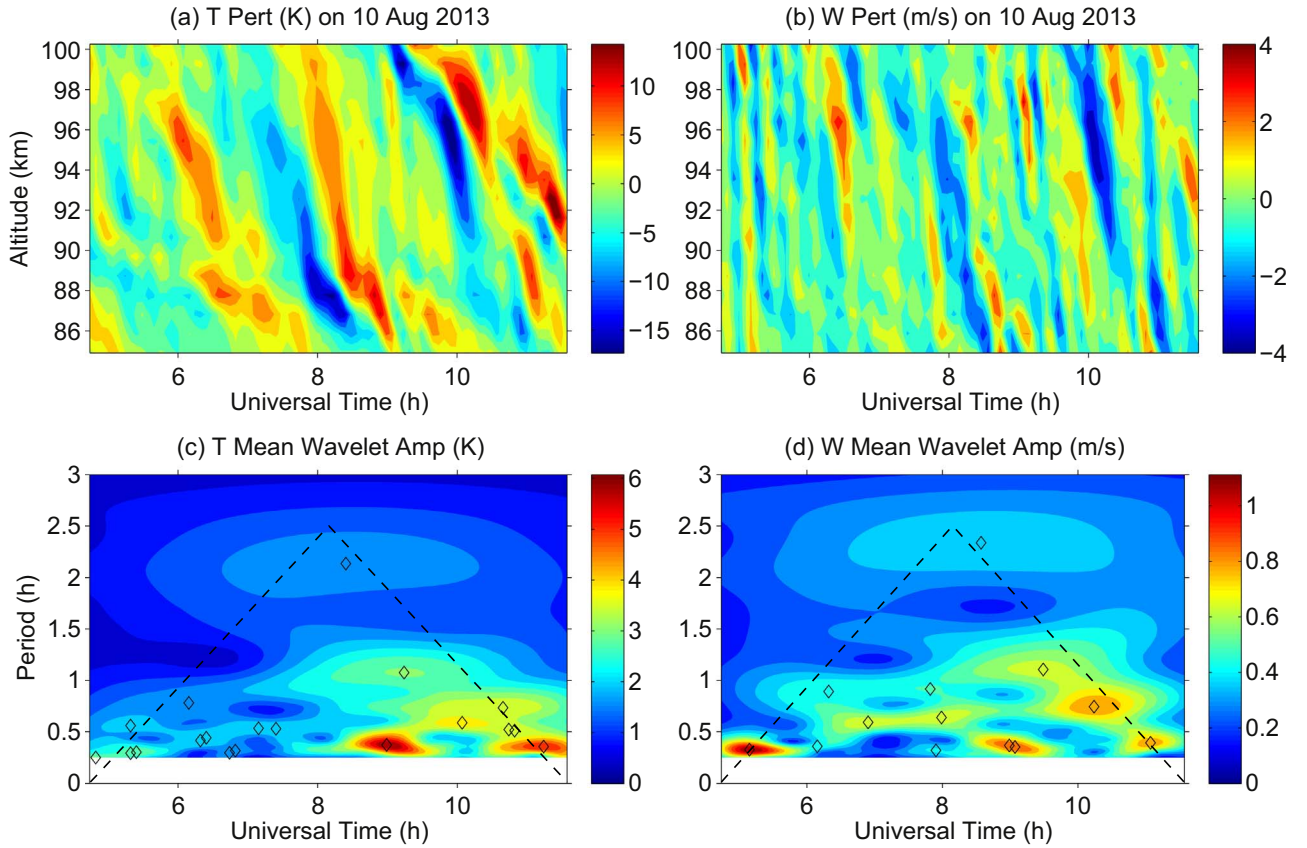


Fig. 2. (a) Temperature and (b) vertical wind perturbations after the 2DFFT filtering with a bandpass of 0.25–3 h in the time domain and 2–123 km in the vertical domain. (c) Weighted wavelet spectra for the temperature averaged from 85 to 100 km. (d) Same as (c) except for the amplitude spectra for the vertical wind.

the same vertical wavelength regardless of whether the wave is observed in the temperature or vertical wind. To overcome this issue, a 2-D sinusoidal fitting method is adapted for this study using the following procedure.

After identifying each wave with an observed frequency of ω from the wavelet analysis, we extract it by applying a 2DFFT filtering with a bandpass of $0.7\text{--}1.3\ \omega$ in the frequency domain and $0.0081\text{--}0.5\ \text{km}^{-1}$ in the vertical wavenumber domain to the wave perturbations that are obtained from only subtracting nightly means. This filtering process selects a quasi-monochromatic wave in the frequency domain that is reflected by its narrow bandwidth in frequency, but allows for multiple peaks in the wavenumber domain because of its wide bandwidth in wavenumber. We then apply a 2DFFT to the filtered wave field that is confined to the duration window of this wave (e.g., Fig. 3a and b) to derive the wave amplitude spectrum as a function of frequency and vertical wavenumber (Fig. 3c and d). The frequency and vertical wavenumber used as the x - and y -axis in Fig. 3c and d are defined and derived as $1/\tau$ and $1/\lambda_z$, where τ and λ_z are the wave period in h and vertical wavelength in km, respectively. Therefore, the frequency and vertical wavenumber have the units of $1/\text{h}$ and $1/\text{km}$, respectively. Multiple peaks in the vertical wavenumber are frequently observed, but only the first two peaks are considered here since the higher-order ones are usually weak. It is interesting to note that on the night of 3 May 2013, the 2DFFT spectra show that the first peak in the vertical wind,

characterized by a long vertical wavelength ($\sim 40\ \text{km}$), corresponds to the secondary peak in relative temperature while the first peak in the temperature, characterized by a short vertical wavelength ($\sim 6\ \text{km}$), corresponds to the secondary peak in the vertical wind (Fig. 3c and d). Here, the first and secondary peaks correspond to the largest and the second largest magnitudes in the 2DFFT spectrum, respectively. This observation is consistent with Fig. 3a and b, which show that the wave fields are superimposed by two different waves with the temperature/vertical wind field being dominated by a short/long vertical wavelength, respectively.

From the 2DFFT spectra, we first identify the peaks for temperature and vertical wind individually, and then apply the following criterion to claim the common peak: the differences must not differ by more than 30% of their means for both frequency and vertical wavenumber. After a common peak is selected, the mean frequency $\bar{\omega}$ and vertical wavenumber \bar{m} are fed into the 2D fitting to derive wave amplitude and phase as follows,

$$\begin{aligned} T'/\bar{T}(t, z) &= A_T \cos(\bar{\omega}t - \bar{m}z - \varphi_T) \\ w'(t, z) &= A_w \cos(\bar{\omega}t - \bar{m}z - \varphi_w), \end{aligned} \quad (2)$$

where A_T and A_w are the amplitudes in the relative temperature (T'/\bar{T}) and vertical wind w' , respectively, and φ_T and φ_w are the corresponding phases. Note that the amplitudes (A_T and A_w) and phases (φ_T and φ_w) are constant within the 2D fitting window. The fitting uncertainties (σ_{A_T} , σ_{A_w} , σ_{φ_T} , σ_{φ_w}) are taken as the standard deviations for these parameters from the fitting processes. The relative temperature perturbations are calculated as the temperature perturbations divided by the mean temperature averaged over the fitting window. Therefore, this mean or background temperature includes the effects of nightly mean, tides, and waves with periods longer than the window length.

Fig. 3e and f show the fitted wave fields that correspond to the first

Table 2
Periods and durations of the waves identified from wavelet spectra for August 10, 2013.

	Wave 1	Wave 2	Wave 3	Wave 4	Wave 5	Wave 6
Period (h)	2.3	1.1	0.78	0.31	0.37	0.38
Duration (UT)	5–12	7.7–11	9.1–11.5	4.7–5.6	8.4–9.6	10.4–11.6

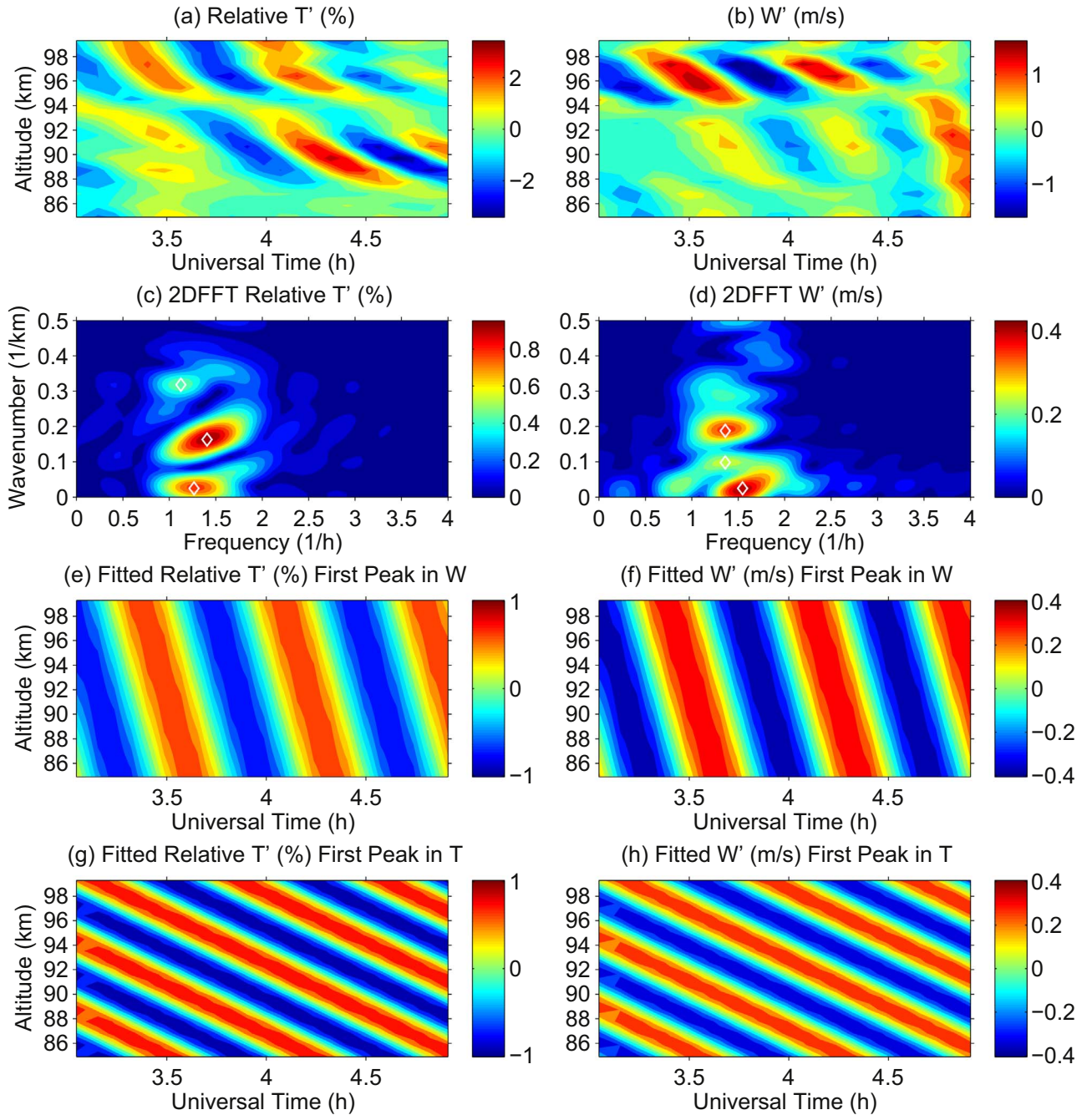


Fig. 3. The filtered wave perturbations in (a) relative temperature and (b) vertical wind on 3 May 2013. (c) and (d) are their 2DFFT amplitude spectra. The white diamonds highlight the spectral peaks. (e) and (f) are the 2D-fitted wave fields corresponding to the first peak in vertical wind and the secondary peak in temperature. (g) and (h) are the same as (e) and (f) except for the first peak in temperature and the secondary peak in vertical wind.

and secondary peaks in vertical wind and relative temperature, respectively. Fig. 3g and h are the same, except for the first peak in relative temperature and the secondary peak in vertical wind. Even before the fitting, the existence of these two waves is discernable in Fig. 3a and b. Although the plane wave formula used in the 2D fitting cannot capture the wave amplitudes varying in time and space, it is sufficient for estimating the average amplitude and phase for a quasi-monochromatic wave. When the wave fields are too complex to be represented by monochromatic waves, the 2D fitting uncertainties are large and these cases are discarded. We only keep the waves satisfying $\sigma_{A_T} < 0.2 \times A_T$, $\sigma_{A_W} < 0.2 \times A_W$, $\sigma_{\varphi_T} < 10^\circ$, $\sigma_{\varphi_W} < 10^\circ$. There are lidar-based observations and numerical modeling efforts illustrating that a

gravity wave packet excited by a source of finite duration and size can evolve from a 1-h wave in temperature perturbations during the early hours into a 1.5-h wave during the second half of the night at Logan, Utah (Yuan et al., 2016). This shift in wave period is also accompanied by a decreasing vertical wavelength. This evolution is a gradual process and, in most cases, it is still reasonable to assume that within 3–4 wave cycles, the wave periods and vertical wavelengths will remain approximately constant. Therefore, the plane wave assumption is valid over our analysis period. Applying these constraints to our dataset yields 184 waves, of which 134 of them have vertical wavelengths that are the first peaks in both vertical wind and temperature and 50 of them involve the secondary peaks.

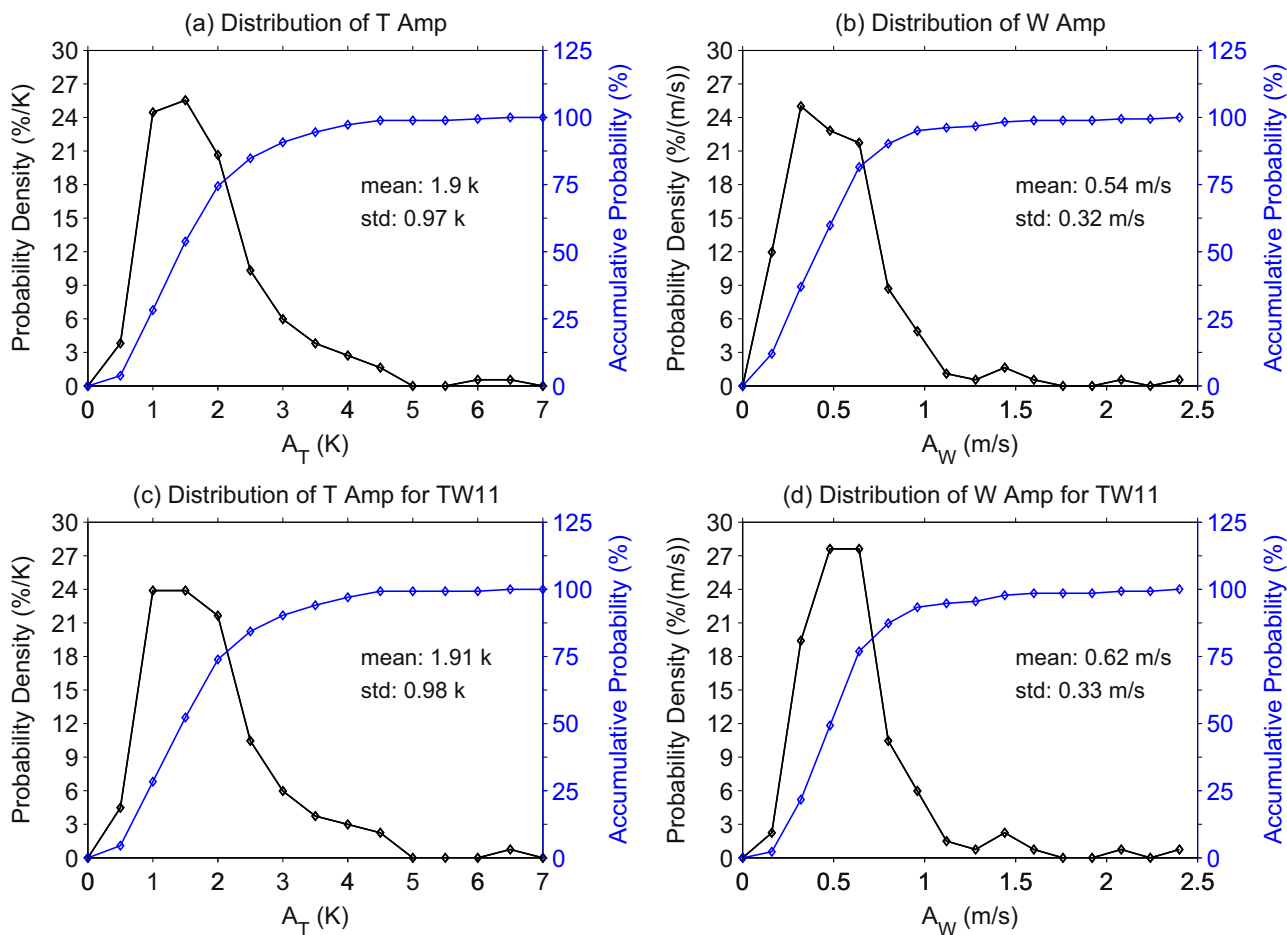


Fig. 4. Probability density functions (black) of wave amplitudes in (a) temperature and (b) vertical wind. The corresponding accumulative probabilities (blue) are plotted on the right axes. (c) and (d) are the same as (a) and (b) except that only the waves having the vertical wavelengths as the first peaks in both the temperature and vertical wind are shown. (For interpretation of the references to color in this figure legend, the reader is referred to the web version of this article.)

3. Statistical results

3.1. Amplitude ratios, phase differences and vertical wavelengths

Fig. 4a and b show the probability density functions (PDFs) and the accumulative density functions of the wave amplitudes in the temperature and vertical wind for all 184 cases. The mean amplitudes are 1.90 ± 0.014 K and 0.54 ± 0.004 m/s, with maxima reaching 6.5 ± 0.3 K and 2.5 ± 0.2 m/s, respectively. Here, the uncertainties of the mean and maximum amplitudes are propagated from the fitting errors. Fig. 4c and d show the same functions, but only including waves with vertical wavelengths from the first peaks in both the temperature and vertical wind. We label these waves as TW11 waves for simplicity. The mean amplitudes of the TW11 waves in the temperature and vertical wind are 1.91 ± 0.016 K and 0.62 ± 0.006 m/s, respectively, which are comparable with the means of all the waves in Fig. 4a and b. The PDF of the wave amplitudes is asymmetric and possesses an extended tail towards relatively rare but large amplitude events. Similar asymmetric distributions of the momentum flux and potential energy from satellite data are explained as being caused by the inherent intermittency of the waves (Baumgaertner and McDonald, 2007; Alexander et al., 2010; Hertzog et al., 2012), i.e., the wave amplitudes are not constant but vary with time scales comparable to those of the wave packets (Chen et al., 2016). The wave amplitude values we find here should be quoted with caution because although the 2D fitting with a fixed period and vertical wavelength and a constant amplitude facilitates the derivation of the wave amplitude and phase in an averaged sense with minimum

uncertainties, it also imposes strong constraints that lead to an underestimation of the wave impacts locally. For instance, the 0.7-h wave shown in Fig. 3a and b can perturb the relative temperature and vertical wind fields with magnitudes as large as $\sim 3.4\%$ and ~ 1.6 m/s locally, while the fitted amplitudes are only around 1% and 0.4 m/s, respectively.

Amplitude ratios (A_T/A_W) with respect to the ground-based observed periods (τ_{obs}) are shown in Fig. 5a. There is an apparent positive correlation between the amplitude ratios and the observed periods. The linear fitting to the correlation is $A_T/A_W = (2.85 \times \tau_{obs} - 0.37)\%$ (the red line in Fig. 5a). The unit of the amplitude ratios is $1/(\text{m/s})$ and that of the observed periods is h for this empirical relation. The correlation coefficient is ~ 0.76 with a 95% confidence interval of (0.70, 0.82). The phase differences ($\varphi_W - \varphi_T$) are centered around $\sim 84^\circ$ and closely follow a Gaussian distribution in Fig. 5b. The directly calculated mean and standard deviation of the phase differences are 84.2° and 26.7° , respectively, which are close to the values of 84.1° and 26.9° obtained from the Gaussian fitting shown as the red line in Fig. 5b. The uncertainty of the mean phase difference that propagates from the fitting errors is $\sim 0.65^\circ$. The distribution of vertical wavelengths is shown in Fig. 5c. The majority of waves have vertical wavelengths of 5–40 km. The mean and standard deviation of the vertical wavelengths are 18.6 and 7.2 km, respectively.

As mentioned in Section 2.3, the dominant peaks in the vertical wavelength for the vertical wind and temperature are often distinct. To investigate whether there is any dependence of the dominant vertical wavelength on the wave components, we separate the waves into four

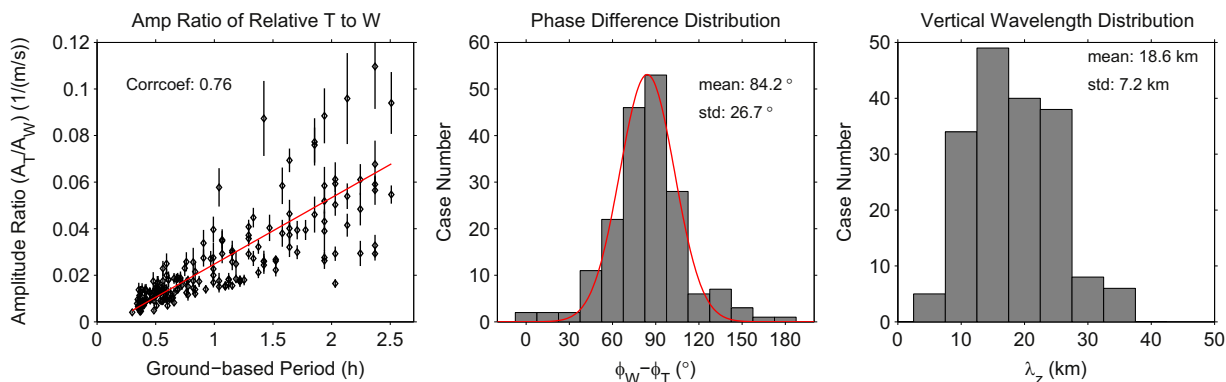


Fig. 5. (a) Amplitude ratios of the relative temperature to the vertical wind with a unit of $1/(m/s)$ versus ground-based periods with a unit of h. The uncertainties of the amplitude ratios propagating from the 2D fitting are plotted as the vertical error bars. The red line represents a linear fitting between the amplitude ratio and the ground-based period. (b) Distribution of the phase differences between the relative temperature and vertical wind ranging from 0° to 180° with an interval of 15° . The red line shows a Gaussian fitting to the distribution with a mean of 84.2° and a standard deviation of 26.7° . (c) Histogram of the vertical wavelengths from 0 to 40 km with a bin size of 5 km. (For interpretation of the references to color in this figure legend, the reader is referred to the web version of this article.)

groups, labeled TW11, TW12, TW21, and TW22, and calculate their means and standard deviations individually (Fig. 6). Following the definition of TW11, the vertical wavelengths of the TW mn waves correspond to those waves with the m th peak in the temperature and the n th peak in the vertical wind. We see that if the first peaks of vertical wavelengths are in vertical winds, they are statistically longer than the first peaks in temperatures, i.e., the mean wavelengths of the TW 21 waves are longer than those of the TW12 waves. The TW11 waves have statistically longer vertical wavelengths than the TW22 waves, implying that shorter-wavelength waves likely experience more dissipation and are thus less dominant.

3.2. Derivation of intrinsic periods and horizontal wavelengths from polarization and dispersion relations with and without dissipation

It is known that molecular viscosity and thermal diffusivity modulate the dispersion and polarization relations of gravity waves, and change the amplitude ratios and phase differences between different wave components (Pitteway and Hines, 1963; Midgley and Liemohn, 1966; Hickey and Cole, 1987; Vadas and Fritts, 2005; Vadas and Nicolls, 2012; Nicolls et al., 2012). In particular, the polarization relation for the temperature and vertical wind perturbations in the presence of molecular viscosity and thermal diffusivity for the f -plane

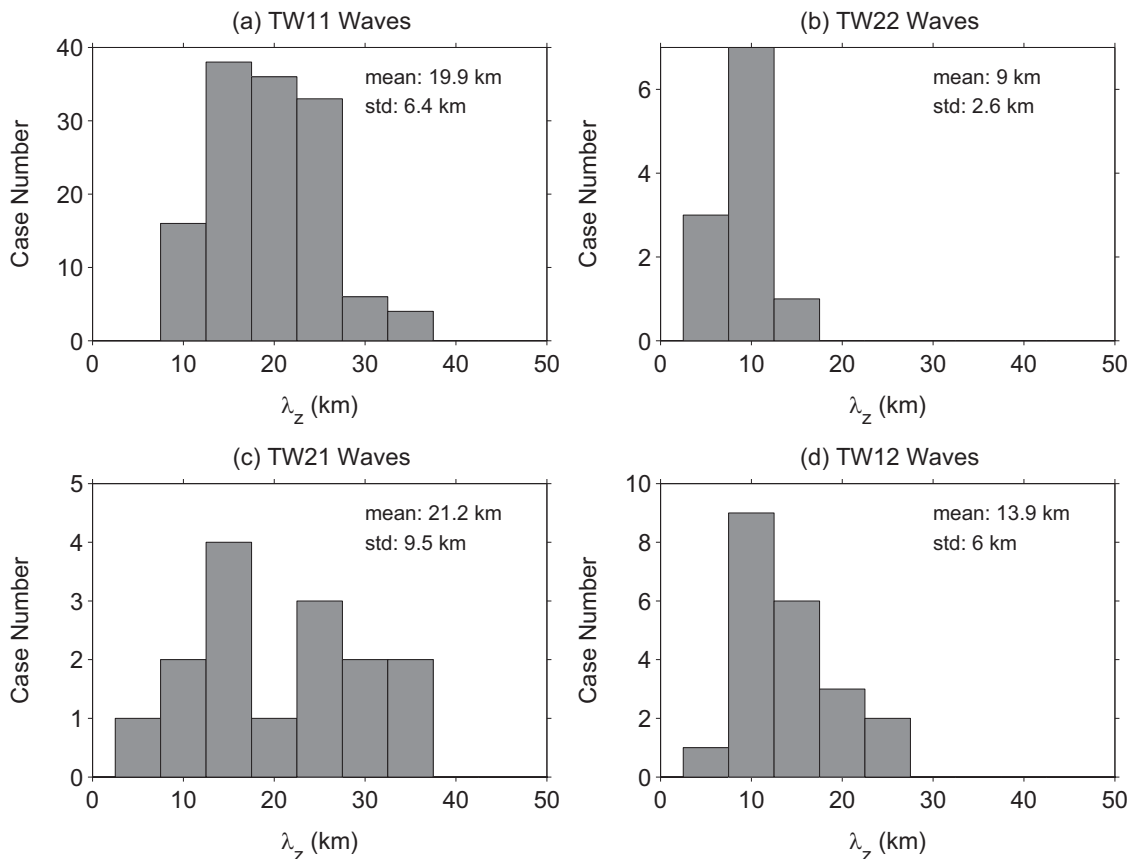


Fig. 6. Distribution of the vertical wavelengths from 0 to 40 km with an interval of 5 km for (a) TW11, (b) TW22, (c) TW21, and (d) TW12 waves. The definition of the TW11, TW12, TW21 and TW22 waves is given in the text.

assumption when the Coriolis force can be neglected (i.e., $f=0$) is given by Eq. (16) in Vadas and Nicolls (2012). Neglecting f is reasonable if the gravity wave's period is much smaller than the inertial period, which is generally true in the thermosphere (Vadas, 2007).

In the thermosphere, molecular viscosity and thermal diffusivity are the dominant dissipative processes for high-frequency gravity waves. However, “eddy” dissipation is the main dissipative mechanism in the mesosphere. Eddy dissipation is created by the turbulence which is formed when previous gravity waves overturn/break/dissipate. In order to adapt Eq. (16) in Vadas and Nicolls (2012) for gravity waves in the mesosphere, we assume that this turbulence is isotropic, which is a reasonable assumption in a well-mixed atmosphere. We then replace the coefficient of the bulk molecular viscosity with the eddy viscosity coefficient via an argument that the eddy viscosity is a rescaled analogy of the molecular viscosity (Holloway, 1997). Then the eddy viscosity formulas are the same as the molecular viscosity formulas (e.g., Liu et al., 2000; Liu et al., 2009; Smith et al., 2011). In order to only include the bulk viscosity, we set $a = b = 0$ in Eq. (16) in Vadas and Nicolls (2012). Additionally, we assume that the eddy viscosity is constant over our altitude range, which is typically ~ 15 – 25 km. In order to be consistent with our definition of the wave phase in Eq. (2), we replace i with $-i$ in Eq. (16) of Vadas and Nicolls (2012). This prescription for the replacement was discussed in Appendix B of Vadas (2013). We substitute ν (the kinematic molecular viscosity) in Eq. (16) of Vadas and Nicolls (2012) with K , which we define as the kinematic eddy viscosity. Then, the polarization relation between the relative temperature and the vertical wind under the influence of eddy viscosity and diffusion is:

$$\tilde{T}/\tilde{W} = \frac{(\gamma - 1)}{C_s^2 D} \left[\gamma i \omega_l (i \omega_l - \alpha K) + \frac{C_s^2}{H} \left(-im + \frac{1}{2H} \right) \right], \quad (3)$$

and

$$D = \left[i \omega_l \left(\gamma im - \frac{1}{H} + \frac{\gamma}{2H} \right) + \frac{\gamma \alpha K}{Pr} \left(-im + \frac{1}{2H} \right) \right], \quad (4)$$

$$\alpha = -(k_H^2 + m^2) + \frac{1}{4H^2} - \frac{im}{H}, \quad (5)$$

where $\tilde{T}/\tilde{W} = A_T \exp(-i\varphi_T)$ and $\tilde{W} = A_W \exp(-i\varphi_W)$ are the complex relative temperature and vertical wind perturbations, A_T and A_W are the corresponding (real) amplitudes, φ_T and φ_W are the corresponding phases, ω_l is the intrinsic frequency which includes both the real and imaginary parts, and k_H and m are the horizontal and vertical wavenumbers, respectively. In the mesosphere, the specific heat ratio is $\gamma = 1.4$ (Kundu, 1990) and the gravitational acceleration is $g = 9.5$ m/s². Additionally, H and C_s are the scale height and sound speed, which are related to the background temperature via $H = R\bar{T}/g$ and $C_s = \sqrt{\gamma R\bar{T}}$, respectively. \bar{T} is the mean temperature obtained from the lidar measurements. The Prandtl number (Pr) is the ratio of the viscous diffusion rate to the thermal diffusion rate and we use a value of $Pr = 1$ for the current study. The amplitude ratio (A_T/A_W) is determined from the absolute value of \tilde{T}/\tilde{W} while the phase difference ($\varphi_W - \varphi_T$) is determined from the inverse tangent of the ratio of the imaginary to the real parts of \tilde{T}/\tilde{W} .

Using Eq. (3), the amplitude ratio and phase difference can be determined from ω_l , k_H , m and K . A gravity wave within a wave packet decays explicitly in time from dissipation. Therefore, we fix the vertical wavenumber to be real, so that the intrinsic frequency consists of both real and imaginary parts (Eq. (24) in Vadas and Fritts, 2005 (VF05)):

$$\omega_l = \omega_{lr} - i\omega_{li}. \quad (6)$$

Here, ω_{lr} is the real part and equals the intrinsic frequency of the gravity wave via the dispersion relation and ω_{li} is the imaginary part and relates to the inverse decay rate of the wave amplitude with time due to dissipation. Here, we have substituted i with $-i$ as well. By knowing the wave's vertical and horizontal wavelengths as well as eddy

viscosity, the inverse decay rate can be calculated using Eq. (25) in VF05:

$$\omega_{li} = -\frac{K}{2} \left(k_H^2 + m^2 - \frac{1}{4H^2} \right) \frac{[1 + (1 + 2\delta)/Pr]}{(1 + \delta_+/2)} \quad (7)$$

and the gravity wave dispersion relation involving ω_{lr} , k_H , m and K can be written as (Eq. (26) in VF05):

$$\omega_{lr}^2 + \frac{K^2}{4} \left(k_H^2 + m^2 - \frac{1}{4H^2} \right)^2 (1 - Pr^{-1})^2 \frac{(1 + \delta_+ + \delta^2/Pr)}{(1 + \delta_+/2)^2} + \frac{K_+ m \omega_{lr}}{H} + \frac{K^2 m^2}{Pr H^2} = \frac{k_H^2 N^2}{k_H^2 + m^2 + 1/4H^2}. \quad (8)$$

Here $\delta_+ = \delta(1 + Pr^{-1})$, $K_+ = K(1 + Pr^{-1})$ and $\delta = Km/H\omega_{lr}$, and N is the Brunt–Väisälä frequency calculated from the lidar data using Eq. (3) in Lu et al. (2015b). Note that Eqs. (7) and (8) are the anelastic approximation of the full compressible complex dispersion relation given by Eq. (12) in Vadas and Nicolls (2012). We use Eqs. (7) and (8) here because they are simpler to solve numerically and because the waves we analyze here satisfy the anelastic approximation.

In principle, with m known from observations, for each pair of (k_H , K) we can use Eqs. (7) and (8) to solve ω_{lr} and ω_{li} using an iterative method described in Vadas and Nicolls (2012). By substituting all four variables (m , k_H , K , and ω_l) into the polarization relation Eq. (3), the amplitude ratio (A_T/A_W) and the phase difference ($\varphi_W - \varphi_T$) corresponding to a set of (m , k_H , K) or equivalently (m , ω_l , K) can be derived. Therefore, for a given m , there is a one-to-one correspondence between each pair of (ω_l , K) and its corresponding amplitude ratio (A_T/A_W), and a one-to-one correspondence of (ω_l , K) with horizontal wavenumber (k_H). Such correspondences are plotted in Fig. 7a and b, respectively, for a 1.15-h wave observed on 10 August 2013, with ω_{lr} shown on the x-axis. We also overplot the observed amplitude ratio (~ 0.03) as a white line in Fig. 7a. This allows us to obtain the intrinsic frequency as a function of the eddy viscosity (y -axis). For this wave, the amplitude ratio is more sensitive to the intrinsic frequency than to the eddy viscosity: Even as the eddy viscosity changes from 0 to 1000 m²/s, the range of the intrinsic period is quite narrow for a given amplitude ratio. The values of (ω_{lr} , K) constrained by the observed amplitude ratio (the white line in Fig. 7a) are then used in Fig. 7b (white line) to obtain the horizontal wavelength as a function of the eddy viscosity.

The eddy viscosity reported in the literature for the MLT region has a wide range, but is usually less than 800 m²/s (e.g., Gardner and Voelz, 1987; Hocking, 1988; Fukao et al., 1994; Lübken, 1997; Bishop et al., 2004; Liu, 2009). It is valuable to compare the intrinsic period and horizontal wavelength with and without including the eddy viscosity. By setting the eddy viscosity $K = 0$ in Eq. (3), the polarization relation without dissipation can be written as (e.g., Eq. (B11) in Vadas, 2013),

$$\tilde{T}/\tilde{W} = \frac{N^2 (im - \frac{1}{2H}) - \frac{\omega_{lr}^2}{\gamma H} (1 - \gamma)}{g \omega_{lr} \left(m - \frac{i}{2H} + \frac{i}{\gamma H} \right)}. \quad (9)$$

Here, we have used $N^2 = \frac{(\gamma-1)g^2}{C_s^2}$. Note that since there is no dissipation, the imaginary part of the intrinsic frequency is zero and we have $\omega_l = \omega_{lr}$. For our waves of interest, the wave frequencies are much smaller than the buoyancy frequency (i.e., $\omega_{lr}^2 \ll N^2$). If we take the absolute value of both sides, Eq. (9) can be used to estimate ω_{lr} as,

$$\omega_{lr} = \left| \frac{N^2 (im - \frac{1}{2H})/g \left(m - \frac{i}{2H} + \frac{i}{\gamma H} \right)}{|\tilde{T}/\tilde{W}|} \right| \quad (10)$$

The amplitude ratio $|\tilde{T}/\tilde{W}|$ and vertical wavenumber m are obtained from observations. The non-dissipative dispersion relation is then used to derive the horizontal wavelength (Fritts and Alexander, 2003),

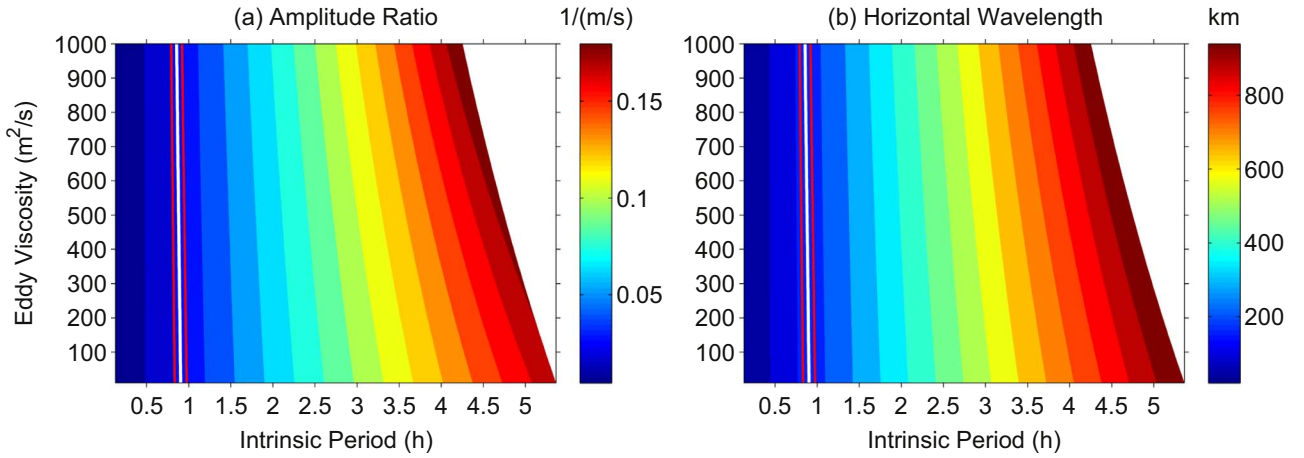


Fig. 7. (a) Amplitude ratios, and (b) horizontal wavelengths as a function of the real parts of intrinsic periods and eddy viscosity coefficients for a 1.15-h wave on 10 August 2013. The vertical wavelength of this wave is ~ 14.4 km. The observed amplitude ratio is overplotted as the white line and the red lines highlight the amplitude ratio $(0.03) \pm$ its uncertainties (0.002) from the 2D fittings. (For interpretation of the references to color in this figure legend, the reader is referred to the web version of this article.)

$$k_H^2 = \frac{\left(m^2 + \frac{1}{4H^2}\right)(\omega_{lr}^2 - f^2)}{N^2 - \omega_{lr}^2} \quad (11)$$

where f is the inertial frequency, corresponding to a period of 18.7 h in Boulder.

3.3. Intrinsic periods, horizontal wavelengths, and phase difference deviations

Fig. 8a–d show the real part of the intrinsic periods versus the ground-based periods for four different eddy viscosities. The intrinsic

periods used in Fig. 8a and e are calculated directly from Eq. (10), while those in Fig. 8b–d and f–h are iteratively derived from Eq. (8) including eddy dissipation. The black diamonds above the red lines represent the waves with intrinsic periods longer than the observed periods and those below the red lines represent the opposite situation. The general distribution patterns of the intrinsic periods are comparable for the different eddy viscosities, although the percentage of the intrinsic frequencies Doppler-shifted to higher frequencies increases from 77.1%, 78.9%, 80.6%, to 81.1%, respectively, for $K = 0, 100, 400, 800$ m^2/s (Fig. 8a–d). This implies that 1) a majority of the waves identified by the wavelet spectra propagate against the mean wind and are blue-shifted to higher intrinsic frequencies; 2) for

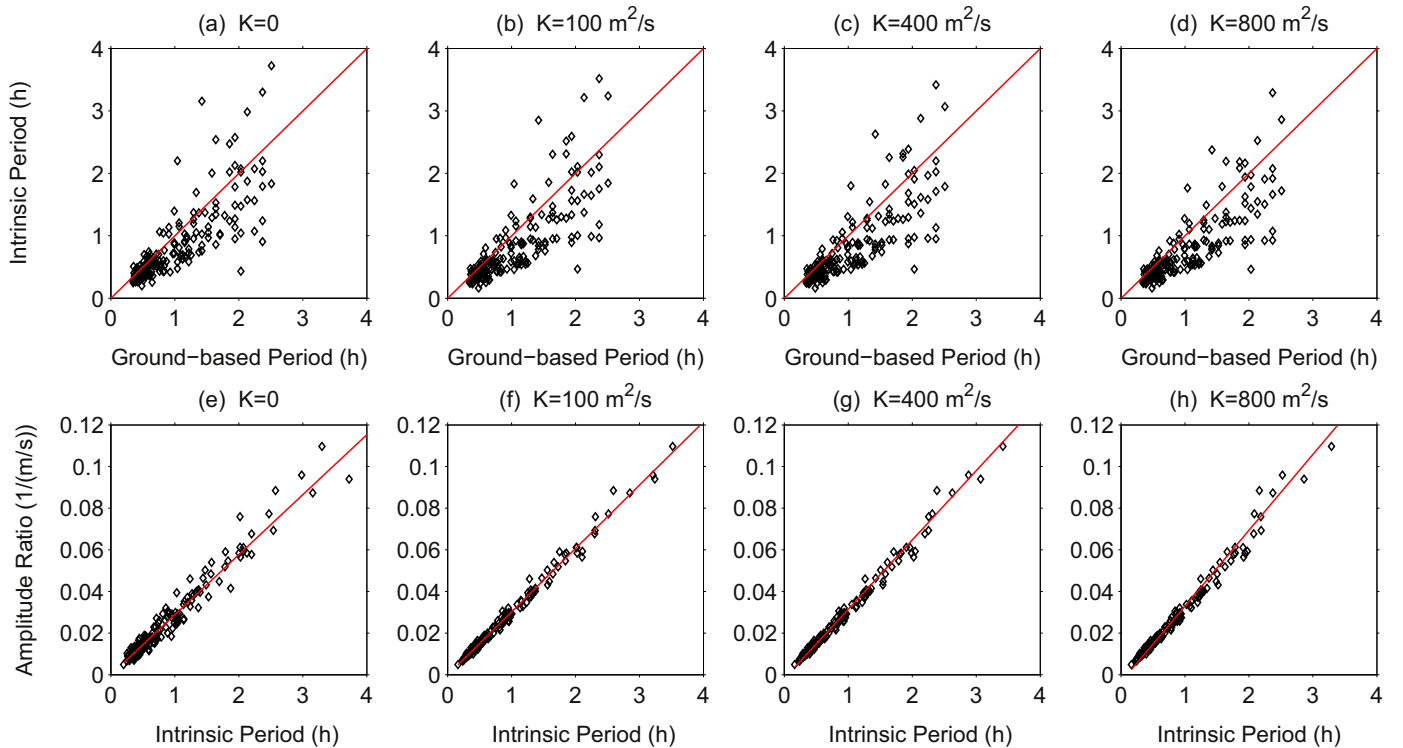


Fig. 8. (a)–(d) The distribution of the real parts of the intrinsic periods as a function of ground-based periods for different eddy viscosities. The red lines correspond to the 1:1 ratio of the intrinsic period to the ground-based period. (e)–(h) Amplitude ratios versus intrinsic periods for different eddy viscosities. The red lines are the linear fittings of the amplitude ratios versus the intrinsic periods. The intrinsic periods in (a) and (e) are derived from Eq. (10) while those in other figures are derived from Eq. (8). (For interpretation of the references to color in this figure legend, the reader is referred to the web version of this article.)

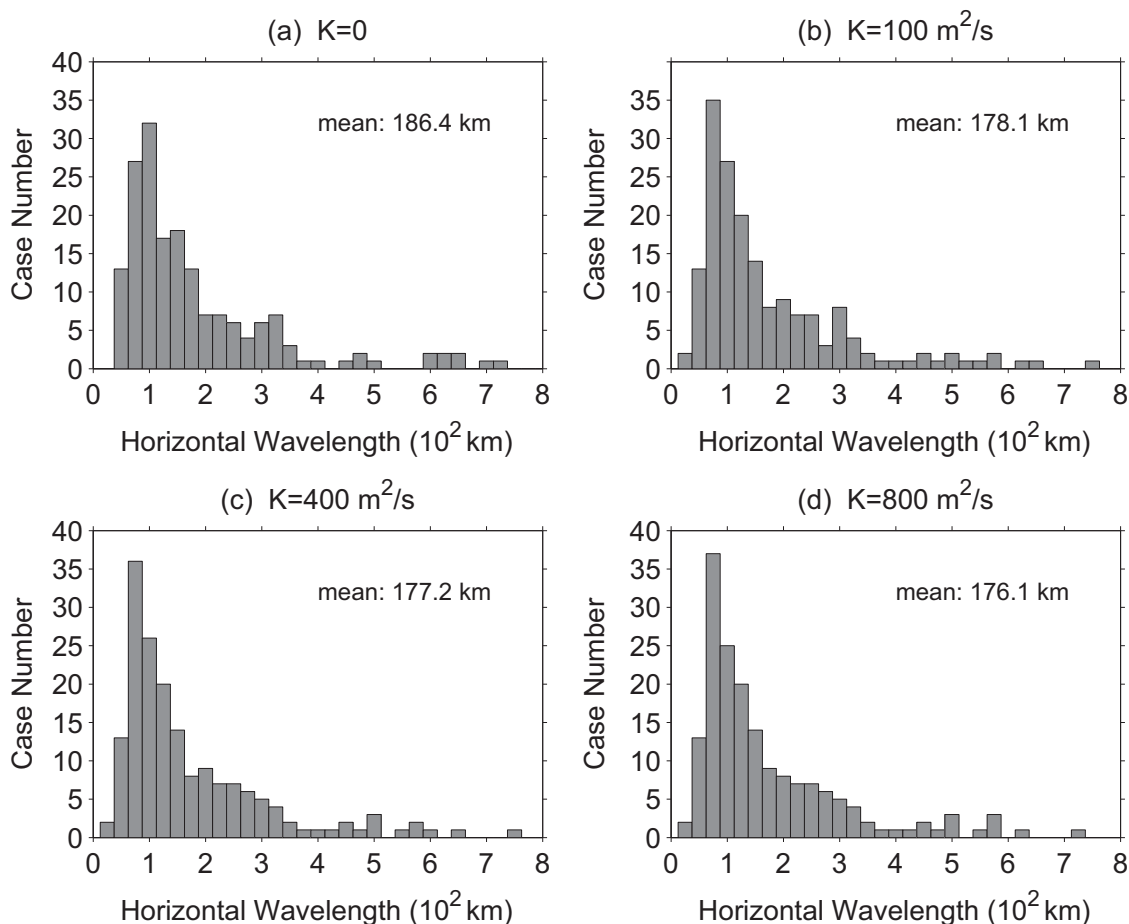


Fig. 9. (a)–(d) The distribution of the horizontal wavelengths for eddy viscosities equal to 0, 100, 400, and 800 m^2/s . The horizontal wavelengths in (a) are computed from Eq. (11), while those for the other three figures are computed from the combination of Eqs. (3)–(8). Please see details in the text.

most of the waves, increasing the eddy viscosity tends to enhance the Doppler-shifting to higher frequencies. This makes sense because when waves propagate against the mean wind, they will have longer vertical wavelengths and experience less dissipation than those waves propagating in the direction of the mean wind. Less dissipation means that a wave's amplitude will be better preserved and, therefore, that this wave will be more likely become dominant.

Figs. 8e–h show the amplitude ratios as a function of their intrinsic periods. A quasi-linear relation between them is expected since this relation is inherently embedded in the wave polarization relation (Eqs. (8) and (10)). On the other hand, the deviations from the fitted linear relation (red line in Fig. 5a) can be possibly attributed to the differences between the ground-based and intrinsic periods, since the ground-based periods are used as the x-axis in Fig. 5a.

The general distributions of the horizontal wavelengths are comparable for the different eddy viscosities (Fig. 9). Most of the waves fall into the mesoscale range in terms of horizontal wavelength, i.e., from 50 to 500 km (Uccellini and Koch, 1987). The mean is around 180 km and the uncertainty of this mean propagating from the fitting errors is ~ 16 – 17 km. The distribution of the horizontal wavelengths is not symmetric and has a long tail towards large values. The median value of the horizontal wavelengths is ~ 125 – 126 km.

Eddy dissipation alters the polarization relation that affects the amplitude ratio and phase difference. The observed phase differences are characterized by a Gaussian distribution with a mean of $\sim 84.2^\circ$ and a large standard deviation of $\sim 26.7^\circ$ (Fig. 5b). However, the expected phase differences for non-dissipative waves are characterized by a much narrower distribution, i.e., they range from ~ 70 – 87° with a mean and standard deviation of 81.6° and 3.3° , respectively (Fig. 10a). From

Eq. (9) and with the condition that $\omega_{ir}^2 \ll N^2$, the expected phase difference for a non-dissipative wave can be simply derived from the ratio of the real and imaginary parts in the term $(im - \frac{1}{2H}) \left(m - \frac{i}{2H} + \frac{i}{\gamma H} \right)$. In this case, the eddy viscosity $K = 0$ is assumed for the non-dissipative waves. The significant differences (or deviations) of the observed phase differences from the predicted values for non-dissipative waves are likely indicative of dissipation effects. We calculate these deviations and examine their relation with respect to the vertical wavelength (Fig. 10b and c), which show that the deviations can be both positive and negative, while waves with shorter vertical wavelengths have larger deviations than those with longer vertical wavelengths. This may suggest that shorter waves experience more eddy dissipation than longer ones, consistent with the previous arguments in Forbes (1982), Fuller-Rowell (1995), and Gavrilov and Kshetvetskii (2014).

4. Summary

In this study 10 months of STAR lidar measurements of vertical winds and temperatures in the MLT at Boulder, Colorado are used to examine the statistics of 0.3–2.5 h waves. Waves with these periods represent the most persistent and dominant perturbations found in the vertical wind field. The characteristics of these waves can be divided into the observed quantities and indirectly inferred parameters. Our systematic data analysis methods for deriving these wave properties include three major stages: 1) to identify the dominant waves, 2) to directly derive the vertical wavelengths, amplitudes, and phases of the dominant waves, and 3) to infer the intrinsic periods and horizontal

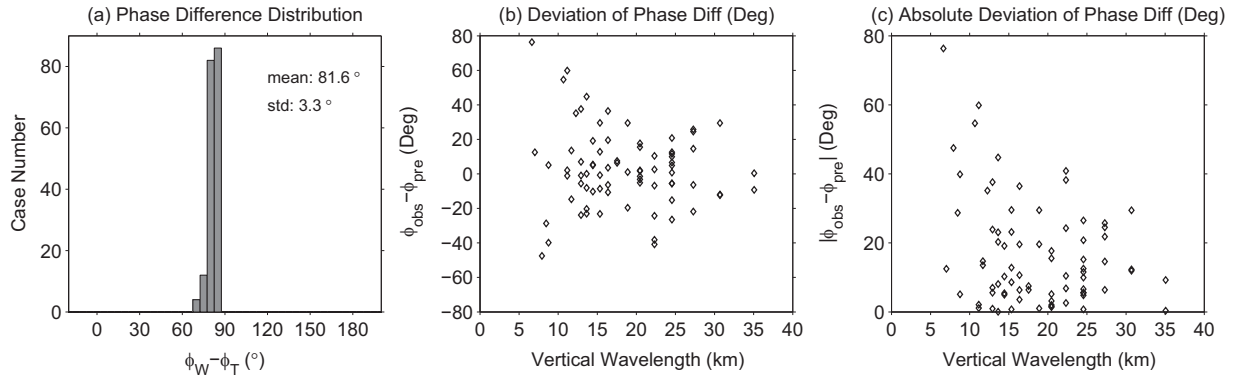


Fig. 10. (a) Phase difference distribution predicted for non-dissipative waves. The interval is 5° . (b) The deviations of the observed phase differences from the predicted values for non-dissipative waves. Each diamond corresponds to one wave case. (c) Same as (b) except for the absolute values of the deviations of the phase differences.

wavelengths using the gravity wave polarization and dispersion relations with and without dissipation. The steps of our methodology are summarized below.

Stage 1 – to identify the dominant waves:

1. The nightly mean temperatures and vertical winds are subtracted from the raw fields to obtain the initial temperature and vertical wind perturbations (T' , W').
2. 2DFFT filtering with a bandpass of $(1/0.25 \text{ h}^{-1}, 1/3 \text{ h}^{-1})$ in the frequency domain and $(0.0081 \text{ km}^{-1}, 0.5 \text{ km}^{-1})$ in the vertical wavenumber domain is applied to (T', W') to derive the filtered perturbations (T'_{filt} , W'_{filt}).
3. A 1D wavelet analysis is applied to the filtered wave perturbations (T'_{filt} , W'_{filt}) to determine the ground-based frequency (ω) of the dominant waves and their durations (t_{start} , t_{end}).

Stage 2 – to determine the vertical wavelength, amplitude, and phase after a wave with a frequency of ω is identified in the time domain:

1. 2DFFT filtering with a bandpass of $(0.7\omega, 1.3\omega)$ in the frequency domain and $(0.0081 \text{ km}^{-1}, 0.5 \text{ km}^{-1})$ in the vertical wavenumber domain is applied to the initial perturbations (T' , W') to obtain the filtered perturbations ($T'_{\text{filt}}(\omega)$, $W'_{\text{filt}}(\omega)$) that are particularly caused by this wave with the frequency of ω .
2. 2DFFT is applied to the filtered perturbations within the wave duration window, i.e., $T'_{\text{filt}}(\omega)[t_{\text{start}}, t_{\text{end}}]$, $W'_{\text{filt}}(\omega)[t_{\text{start}}, t_{\text{end}}]$. The common peaks in the temperature and vertical wind are identified from the 2DFFT spectra. The mean frequency $\bar{\omega}$ and vertical wavenumber \bar{m} are computed. The vertical wavelength is calculated as $2\pi/\bar{m}$.
3. $\bar{\omega}$ and \bar{m} are employed in the 2D fitting to $T'_{\text{filt}}(\omega)[t_{\text{start}}, t_{\text{end}}]$, $W'_{\text{filt}}(\omega)[t_{\text{start}}, t_{\text{end}}]$ to derive the wave amplitudes (A_T , A_W) and phases (φ_T , φ_W).

Stage 3 – to infer the intrinsic periods and horizontal wavelengths of the waves with and without dissipation:

1. For the derivation with dissipation, the observed amplitude ratio (A_T/A_W), vertical wavenumber (m), and a given eddy viscosity (K), are used to determine ω_I , using the polarization relation with dissipation. (m , ω_I , K) are then applied to infer horizontal wavelength due to their one-to-one correspondence.
2. For the derivation without dissipation, the observed amplitude ratio (A_T/A_W) and vertical wavenumber m are used to determine ω_I using the gravity wave polarization relation without dissipation (Eq. (10)). (m , ω_I) are then used to infer the horizontal wavelength using the dispersion relation without eddy viscosity (Eq. (11)).

The directly observed quantities include the distributions of wave

amplitudes in the vertical wind and temperature fields, amplitude ratios and phase differences for these two components of wave perturbations, the distributions of the vertical wavelengths for all the waves, and for the four different groups (i.e., TW11, TW12, TW21, and TW22). The amplitude ratios are positively correlated with their ground-based periods with a correlation coefficient of ~ 0.76 , while the deviations from the linear fitting of these two variables may be explained by the differences between the ground-based and intrinsic periods. The phase differences have a mean value of $\sim 84.2^\circ$ and a larger standard deviation ($\sim 26.7^\circ$) than that expected for non-dissipative waves (3.3°). Wave dissipation may cause the phase differences to significantly deviate from the predications for non-dissipative waves, and this effect is likely larger for shorter vertical wavelength waves. The mean vertical wavelength for all of the waves is $\sim 18.6 \text{ km}$, and it is longer for TW21 waves than TW12 waves. On average, the primary waves (TW11 waves) exhibit longer vertical wavelengths than the secondary waves (TW22 waves).

The indirectly inferred parameters are the intrinsic period and the horizontal wavelength inferred from the measured vertical wavelength and amplitude ratio, given a designated value of eddy viscosity. The wave polarization and dispersion relations with and without eddy viscosity and diffusion are used to infer the intrinsic period and horizontal wavelength for dissipative and non-dissipative waves, respectively. This is the first time that such a method has been applied for MLT waves. Note that this method has been previously applied to gravity waves in the thermosphere (Vadas and Nicolls, 2012; Nicolls et al., 2012). For the eddy viscosity coefficients of $K = 0, 100, 400, 800 \text{ m}^2/\text{s}$, the portions of waves that are blue-Doppler-shifted by the mean wind and have higher intrinsic frequencies than the ground-based ones, are 77.1%, 78.9%, 80.6%, to 81.1%, respectively. This implies that the majority of waves identified by the wavelet spectral analysis propagate against the mean wind. Additionally, we find that increasing the eddy viscosity tends to increase the intrinsic frequency. The horizontal wavelengths are mostly within 50–500 km, which falls into the mesoscale range of gravity waves. Their mean and median values are ~ 180 and 125 km , respectively.

This is the first time (to our knowledge) that the amplitude ratios and the phase differences between the temperature and vertical wind are derived directly from real observations and their statistical characteristics are provided considering a total of 184 gravity waves in the MLT. The high-resolution measurements by the University of Colorado STAR lidar enable us to quantify the characteristics of these high-to-medium frequency and mesoscale gravity waves, which provide a valuable database for the validation of high-resolution GCMs such as the high-resolution Whole Atmosphere Community Climate Model (WACCM), Japanese Atmospheric General circulation model for Upper Atmosphere Research (JAGUAR), and K hlungsborn Mechanistic Circulation Model (KMCM). The vertical information of these waves derived from the range-resolved lidar measurements is

also important and complementary to the horizontal wave information derived from airglow imagers and satellites. The seasonal variations of the wave characteristics and their relations with the potential wave sources and the transition of the background winds are intriguing, which deserve a future work.

Acknowledgement

We sincerely acknowledge Dr. Bob Robinson for his guidance and invaluable discussions in the lidar development and research. We are grateful to Dr. Wentao Huang and Dr. Zhibin Yu for their significant contributions to the STAR lidar data collection, and are grateful to Dr. Weichun Fong, Mr. Brendan Roberts and Mr. Ian Dahlke for their key contributions to the STAR lidar development and instrumentation. The STAR lidar work was supported by NSF CAREER grant ATM-0645584 and CRRL Grant AGS-1136272. Xian Lu's research was supported by the NSF CEDAR Grant AGS-1343106. The work of XC, CC and JAS was partially supported by NSF Grants PLR-1246405, AGS-1115224, and AGS-1452351, and the work of SLV was supported by NSF Grant PLR-1246405. The data used in this paper can be requested from the corresponding authors (xianl@clemsun.edu and xinzha.chu@colorado.edu).

References

Alexander, M.J.A., et al., 2010. Recent developments in gravity-wave effects in climate models and the global distribution of gravity-wave momentum flux from observations and models. *Q. J. R. Meteorol. Soc.* 136, 1103–1124.

Baumgaertner, A.J.G., McDonald, A.J., 2007. A gravity wave climatology for Antarctica compiled from Challenging Minisatellite Payload/Global Positioning System (CHAMP/GPS) radio occultations. *J. Geophys. Res.* 112, D05103. <http://dx.doi.org/10.1029/2006JD007504>.

Becker, E., 2009. Sensitivity of the upper mesosphere to the Lorenz energy cycle of the troposphere. *J. Atmos. Sci.* 66, 647–666. <http://dx.doi.org/10.1175/2008JAS2735.1>.

Bishop, R.L., Larsen, M.F., Hecht, J.H., Liu, A.Z., Gardner, C.S., 2004. TOMEX: mesospheric and lower thermospheric diffusivities and instability layers. *J. Geophys. Res.* 109, D02S03. <http://dx.doi.org/10.1029/2002JD003079>.

Chen, C., Chu, X., McDonald, A.J., Vadas, S.L., Yu, Z., Fong, W., Lu, X., 2013. Inertia-gravity waves in Antarctica: a case study using simultaneous lidar and radar measurements at McMurdo/Scott Base (77.8°S, 166.7°E). *J. Geophys. Res. Atmos.* 118, 2794–2808. <http://dx.doi.org/10.1002/jgrd.50318>.

Chen, C., Chu, X., Zhao, J., Roberts, B.R., Yu, Z., Fong, W., Lu, X., Smith, J.A., 2016. Lidar observations of persistent gravity waves with periods of 3–10h in the Antarctic middle and upper atmosphere at McMurdo (77.83°S, 166.67°E). *J. Geophys. Res. Space Phys.* 121. <http://dx.doi.org/10.1002/2015JA022127>.

Collins, R.L., Nomura, A., Gardner, C.S., 1994. Gravity waves in the upper mesosphere over Antarctica: lidar observations at the South Pole and Syowa. *J. Geophys. Res.* 99 (D3), 5475–5485. <http://dx.doi.org/10.1029/93JD03276>.

Forbes, J.M., 1982. Atmospheric tide: 2. The solar and lunar semidiurnal components. *J. Geophys. Res.* 87 (A7), 5241–5252. <http://dx.doi.org/10.1029/JA087iA07p05241>.

Fritts, D.C., Nastrom, G.D., 1992. Sources of mesoscale variability of gravity waves. Part II: frontal, convective, and jet stream excitation. *J. Atmos. Sci.* 49, 111–127.

Fritts, D.C., Alexander, M.J., 2003. Gravity wave dynamics and effects in the middle atmosphere. *Rev. Geophys.* 41, 1003. <http://dx.doi.org/10.1029/2001RG000106>.

Fuller-Rowell, T.J., 1995. The dynamics of the lower thermosphere, the upper mesosphere and lower thermosphere: a review of experiment and theory. In: Johnson, M., Killeen, T.L. (Eds.), *Geophysical Monograph Series*, vol. 87R, AGU, Washington, DC, pp. 23–36.

Fukao, S., Yamanaka, M.D., Ao, N., Hocking, W.K., Sato, T., Yamamoto, M., Nakamura, T., Tsuda, T., Kato, S., 1994. Seasonal variability of vertical eddy diffusivity in the middle atmosphere: 1. Three-year observations by the middle and upper atmosphere radar. *J. Geophys. Res.* 99 (D9), 18973–18987. <http://dx.doi.org/10.1029/94JD00911>.

Gardner, C.S., Voezel, D.G., 1987. Lidar studies of the nighttime sodium layer over Urbana, Illinois, 2. Gravity waves. *J. Geophys. Res.* 92, 4673–4694.

Gavrilov, N.M., Fukao, S., Nakamura, T., Tsuda, T., Yamanaka, M.D., Yamamoto, M., 1996. Statistical analysis of gravity waves observed with the middle and upper atmosphere radar in the middle atmosphere, 1. Method and general characteristics. *J. Geophys. Res.* 101, 29,511–29,521.

Gavrilov, N.M., Kshetvetskii, S.P., 2014. Three-dimensional numerical simulation of nonlinear acoustic-gravity wave propagation from the troposphere to the thermosphere. *Earth Planets Space*, 66–88. <http://dx.doi.org/10.1186/1880-5981-66-88>.

Hertzog, A., Alexander, M.J., Plougonven, R., 2012. On the intermittency of gravity-wave momentum flux in the stratosphere. *J. Atmos. Sci.* 69, 3433–3448.

Hickey, M.P., Cole, K.D., 1987. A quartic dispersion equation for internal gravity waves in the thermosphere. *J. Atmos. Terr. Phys.* 49, 889–899.

Hocking, W.K., 1988. Two years of continuous measurements of turbulence parameters in the upper mesosphere and lower thermosphere made with a 2-MHz radar. *J. Geophys. Res.* 93, 2475–2491. <http://dx.doi.org/10.1029/JD093iD03p02475>.

Holloway, G., 1997. Ocean circulation, Flow in probability under statistical dynamical forcing. In: Molchanov, S.A., Woyczynski, W.A. (Eds.), *Stochastic Models in Geosystems*, Springer-Verlag, New York, pp. 137–148.

Hu, X., Liu, A.Z., Gardner, C.S., Swenson, G.R., 2002. Characteristics of quasi-monochromatic gravity waves observed with Na lidar in the mesopause region at Starfire Optical Range, NM. *Geophys. Res. Lett.* 29 (24), 2169. <http://dx.doi.org/10.1029/2002GL014975>.

Koch, S., O'Handly, C., 1997. Operational forecasting and detection of mesoscale gravity waves. *Weather Forecast.* 12, 253–281.

Kundu, P., 1990. *Fluid Mechanics*. Academic Press, San Diego, 638.

Li, Z., Liu, A.Z., Lu, X., Swenson, G.R., Franke, S.J., 2011. Gravity wave characteristics from OH airglow imager over Maui. *J. Geophys. Res.* 116, D22115. <http://dx.doi.org/10.1029/2011JD015870>.

Liu, A.Z., 2009. Estimate eddy diffusion coefficients from gravity wave vertical momentum and heat fluxes. *Geophys. Res. Lett.* 36, L08806. <http://dx.doi.org/10.1029/2009GL037495>.

Liu, H.-L., Hagan, M.E., Roble, R.G., 2000. Local mean state changes due to gravity wave breaking modulated by the diurnal tide. *J. Geophys. Res.* 105 (D10), 12,381–12,396.

Liu, H.-L., Marsh, D.R., She, C.-Y., Wu, Q., Xu, J., 2009. Momentum balance and gravity wave forcing in the mesosphere and lower thermosphere. *Geophys. Res. Lett.* 36, L07805. <http://dx.doi.org/10.1029/2009GL037252>.

Liu, H.L., McInerney, J.M., Santos, S., Lauritzen, P.H., Taylor, M.A., Pedatella, N.M., 2014. Gravity waves simulated by high-resolution whole atmosphere community climate model. *Geophys. Res. Lett.* 41, 9106–9112. <http://dx.doi.org/10.1002/2014GL024668>.

Lu, X., Liu, A.Z., Swenson, G.R., Li, T., Leblanc, T., McDermaid, I.S., 2009. Gravity wave propagation and dissipation from the stratosphere to the lower thermosphere. *J. Geophys. Res.* 114, D11101. <http://dx.doi.org/10.1029/2008JD011012>.

Lu, X., Chen, C., Huang, W., Smith, J.A., Chu, X., Yuan, T., Pautet, P.-D., Taylor, M.J., Gong, J., Cullens, C.Y., 2015a. A coordinated study of 1h mesoscale gravity waves propagating from Logan to Boulder with CRRL Na Doppler lidars and temperature mapper. *J. Geophys. Res. Atmos.* 120, 10,006–10,021. <http://dx.doi.org/10.1002/2015JD023604>.

Lu, X., Chu, X., Fong, W., Chen, C., Yu, Z., Roberts, B.R., McDonald, A.J., 2015b. Vertical evolution of potential energy density and vertical wave number spectrum of Antarctic gravity waves from 35 to 105km at McMurdo (77.8°S, 166.7°E). *J. Geophys. Res. Atmos.* 120, 2719–2737. <http://dx.doi.org/10.1002/2014JD022751>.

Lübken, F.-J., 1997. Seasonal variation of turbulent energy dissipation rates at high latitudes as determined by in situ measurements of neutral density fluctuations. *J. Geophys. Res.* 102, 13,441–13,456.

Midgley, J.E., Liemohn, H.B., 1966. Gravity waves in a realistic atmosphere. *J. Geophys. Res.* 71, 3729–3748.

Nicolls, M.J., Vadas, S.L., Meriwether, J.W., Conde, M.G., Hampton, D., 2012. The phases and amplitudes of gravity waves propagating and dissipating in the thermosphere: application to measurements over Alaska. *J. Geophys. Res.* 117, A05323. <http://dx.doi.org/10.1029/2012JA017542>.

Pitteway, M.L.V., Hines, C.O., 1963. The viscous damping of atmospheric gravity waves. *Can. J. Phys.* 41, 1935–1948.

Riggin, D., Fritts, D.C., Fawcett, C.D., Kudeki, E., Hitchman, M.H., 1997. Radar observations of gravity waves over Jicamarca, Peru, during the CADRE campaign. *J. Geophys. Res.* 102 (D22), 26263–26281.

Sato, K., Tateno, S., Watanabe, S., Kawatani, Y., 2012. Gravity wave characteristics in the southern hemisphere revealed by a high-resolution middle-atmosphere general circulation model. *J. Atmos. Sci.* 69, 1378–1396. <http://dx.doi.org/10.1175/JAS-d-11-0101.1>.

Smith, A.K., Garcia, R.R., Marsh, D.R., Richter, J.H., 2011. WACCM simulations of the mean circulation and trace species transport in the winter mesosphere. *J. Geophys. Res.* 116, D20115. <http://dx.doi.org/10.1029/2011JD016083>.

Smith, J.A., Chu, X., 2015. High-efficiency receiver architecture for resonance-fluorescence and Doppler lidars. *Appl. Opt.* 54 (11), 3173–3184. <http://dx.doi.org/10.1364/AO.54.003173>.

Suzuki, S., Shiokawa, K., Otsuka, Y., Ogawa, T., Wilkinson, P., 2004. Statistical characteristics of gravity waves observed by an all-sky imager at Darwin, Australia. *J. Geophys. Res.* 109, D20S07. <http://dx.doi.org/10.1029/2003JD004336>.

Taylor, M.J., Pendleton, W.R., Jr., Clark, S., Takahashi, H., Gobbi, D., 1997. Image measurements of short-period gravity waves at equatorial latitudes. *J. Geophys. Res.* 102, 26283–26299.

Torrence, C., Compo, G.P., 1998. A practical guide to wavelet analysis. *Bull. Am. Meteorol. Soc.* 79, 61–78.

Uccellini, L.W., Koch, S.E., 1987. The synoptic setting and possible energy sources for mesoscale wave disturbances. *Mon. Weather Rev.* 115, 721–729.

Vadas, S.L., Fritts, D.C., 2005. Thermospheric responses to gravity waves: influences of increasing viscosity and thermal diffusivity. *J. Geophys. Res.* 110, D15103. <http://dx.doi.org/10.1029/2004JD005574>.

Vadas, S.L., 2007. Horizontal and vertical propagation and dissipation of gravity waves in the thermosphere from lower atmospheric and thermospheric sources. *J. Geophys. Res.* 112, A06305. <http://dx.doi.org/10.1029/2006JA011845>.

Vadas, S.L., Nicolls, M.J., 2012. The phases and amplitudes of gravity waves propagating and dissipating in the thermosphere: theory. *J. Geophys. Res.* 117, A05322. <http://dx.doi.org/10.1029/2011JA017426>.

Vadas, S.L., 2013. Compressible f-plane solutions to body forces, heatings, and coolings, and application to the primary and secondary gravity waves generated by a deep convective plume. *J. Geophys. Res. Space Phys.* 118, 2377–2397. <http://dx.doi.org/10.1029/2012JA017426>.

- 10.1002/jgra.50163.
- Walterscheid, R.L., Hecht, J.H., Vincent, R.A., Reid, I.M., Woithe, J., Hickey, M.P., 1999. Analysis and interpretation of airglow and radar observations of quasi-monochromatic gravity waves in the upper mesosphere and lower thermosphere over Adelaide, Australia (35°S, 138°E). *Atmos. Sol. Terr. Phys.* 61, 461–478.
- Watanabe, S., Miyahara, S., 2009. Quantification of the gravity wave forcing of the migrating diurnal tide in gravity wave-resolving general circulation model. *J. Geophys. Res.* 114, D07110. <http://dx.doi.org/10.1029/2008JD011218>.
- Yuan, T., et al., 2016. Evidence of dispersion and refraction of a spectrally broad gravity wave packet in the mesopause region observed by the Na lidar and Mesospheric Temperature Mapper above Logan, Utah. *J. Geophys. Res. Atmos.* 121, 579–594. <http://dx.doi.org/10.1002/2015JD023685>.
- Zhang, F., 2004. Generation of mesoscale gravity waves in the upper-tropospheric jet-front systems. *J. Atmos. Sci.* 61, 440–457.